

A Multi-Objective Robust Aircraft Wing Shape Optimization Approach

Gorkem Demir¹ and Recep M. Gorguluarslan²

*TOBB University of Economics and Technology, Department of Mechanical Engineering,
Cankaya, Ankara, 06560, Turkey*

Selin Aradag³

TED University, Department of Mechanical Engineering, Kolej, Ankara, 06420, Turkey

A robust aerodynamic shape optimization problem is one of the most challenging processes due to the high number of design parameters. The consideration of uncertainties causes a considerable computational burden. Therefore, the reduction of the number of required design variables has a significant impact on computational efficiency. In this study, Proper Orthogonal Decomposition (POD) method is utilized to extract the essential feature of the design variables for an aircraft wing geometry. The design exploration is conducted with the reduced-order parametric model constructed with POD rather than using the more complex or high-dimensional system. The Radial Basis Function (RBF) interpolation technique is implemented to estimate the unknown field available in the design space. Model-form uncertainties originating from the turbulence model required for the CFD analyses are determined using the eigenspace perturbation methodology. Robust solutions that satisfy the design requirements are obtained while taking uncertainties into account using Inductive Design Exploration Method (IDEM). The results of the case study show that geometric filtration using POD-RBF based IDEM computation approach is an alternative multi-objective robust optimization framework.

I. Nomenclature

AOA	=	Angle of Attack
β	=	Side-Slip Angle
CD	=	Drag Coefficient
CL	=	Lift Coefficient
CFD	=	Computational Fluid Dynamics
CR- β	=	Rolling Moment Coefficient Gradient
DACE	=	Design, and Analysis of Computer Experiments
DC	=	Drag Count (1 DC = 0.0001 drag coefficient)
IDEM	=	Inductive Design Exploration Method
LHS	=	Latin Hypercube Sampling
POD	=	Proper Orthogonal Decomposition
RANS	=	Reynold's Averaged Navier-Stokes
RBF	=	Radial Basis Function
SST	=	Shear Stress Transport

¹ Ph.D. Student, Mechanical Engineering
² Assistant Professor, Mechanical Engineering
³ Professor, Mechanical Engineering, AIAA Senior Member

II. Introduction

Aerodynamic shape optimization is a primary topic for the aviation industry to achieve diverse design requirements. Since the development of a novel and reliable optimization framework has received more attention in recent years with the advancements in powerful computer algorithms and numerical methods, researchers have focused on multi-point and multi-objective design exploration [1].

Geometry parametrization is one of the most fundamental and essential procedures to obtain various design alternatives effortlessly available in the desired design space [2-7]. In this study, Bezier curve that is one of the most popular computer-aided design methods is used to manipulate the airfoil geometry, and wing surface parametrization is accomplished with a Bezier surface that is composed of the Bezier curves [6]. There are several design variables in the parametrization process. Proper Orthogonal Decomposition (POD), which is a statistical technique to reduce the higher system dimensions to simple approximate description, is implemented in the parametrization procedure [8-12]. The wing geometry control is handled with the POD coefficients that can be denoted as the dominant features of the wing geometry instead of the original design variables.

The computational burden originating from the evaluation of the true response of the sampled points required for the design exploration is still a problem. Surrogate model can be an alternative way to enrich the design space to overcome this problem. Since POD has no predictive feature for the unknown field of the design space individually, Radial Basis Function (RBF) that is an interpolation technique is implemented to accompany POD to establish a functional relationship between the input and output parameters [18, 19].

Turbulent flows have an important role in aerodynamic design studies. Reynolds Averaged Navier-Stokes (RANS)-based turbulent models are widely preferred for aerodynamic simulations. Model-form uncertainty quantification originating from the RANS-based turbulent models attempts to assess the trustworthiness of model predictions of quantities of interest. Eigenspace perturbation methodology available in the literature is used by perturbing the Reynolds stress [21-23].

Multi-objective design problems become more complicated with considering the uncertainties to obtain robust solutions. The objective of this study is to propose a robust optimization approach called Inductive Design Exploration Method (IDEM) which is a recursive process that links multiple design levels to determine the combinations of input parameters that provide robust solutions to the ranged set of requirements specified for top-level performance parameters [24]. An improved Inductive Design Exploration Method (IDEM) is introduced to the aerodynamic field to find optimal design range for specified performance conditions by adopting the POD approach for design variable reduction and response surface modeling in the robust optimization process under epistemic modeling uncertainties to overcome this issue [24-26].

III. Theoretical Background

A. Definition of Bezier Curves and Surfaces

Geometry parameterization has a significant role to manipulate airfoil and wing geometries to explore the optimum geometries available in a design space that satisfy the design criteria. In this study, Bezier curves that are the parametric curves to generate a wide range of geometrical shapes required for aerospace applications are preferred to identify the mathematical definition of the airfoils [27]. An n -th order Bezier curve is defined as;

$$z(t) = \sum_{i=0}^n B_i^n(t) P_i \quad (1)$$

where $B_i^n(u)$ is the Bernstein polynomial that is described in Eq. 2, P_i is the matrix that contains $n+1$ control points and t is the curvilinear coordinate. Any control points along the curve have a significant effect on curve segments, and these segments are specified through the order of the curve. Thus, the accuracy of Bezier curves is highly affected by the degree of the polynomial.

$$B_{i,n}(u) = \frac{n!}{i!(n-i)!} u^i (1-u)^{n-i} \quad (2)$$

Bezier surfaces that are composed of Bezier curves are used to parametrize the wing surfaces. Instead of polygon characteristics, Bezier surfaces have polyhedron characteristics that can be defined in Eq. 3.

$$p(u, w) = \sum_{i=0}^m \sum_{j=0}^n P_{ij} B_{i,m}(u) B_{j,n}(w) \quad (3)$$

where P_{ij} is the array of vertices in the control polyhedron, u and w are the parameters identifying surface patch in the range of $[0,1]$.

B. Proper Orthogonal Decomposition Theory

Proper Orthogonal Decomposition (POD) is a data reduction procedure to transform a problem from a complex and high-dimensional dataset into a simple approximate description by extracting the dominant features of the given dataset. The ensemble set of observations organized as a snapshot matrix that consists of geometrical coordinates of M candidate wings in this study can be expressed as [28];

$$S_j = [S_1, S_2, \dots, S_M], j = 1, 2, \dots, M \quad (4)$$

where S is the snapshot matrix. The deviations of the snapshot matrix (V_j) are extracted from its mean value to prevent scaling requirement for further applications [29-30].

$$V_j = [S_1 - \bar{S}, S_2 - \bar{S}, \dots, S_M - \bar{S}] \quad (5)$$

\bar{S} is the mean value of the snapshot matrix. The procedure is followed by computing the correlation matrix that is defined as the integral of the inner product of the deviation at different points of the snapshot matrix. The correlation matrix is a non-negative matrix that includes eigenvalues and orthogonal eigenvectors. Singular Value Decomposition (SVD) method is used to obtain the eigenvalues and eigenvectors of a correlation matrix given by;

$$[R] = [C][\Sigma][P]^T = [C] \begin{bmatrix} \sigma_1 & \dots & 0 \\ \vdots & \ddots & \vdots \\ 0 & \dots & \sigma_M \end{bmatrix} [P]^T \quad (6)$$

where $[C]$ is the orthogonal eigenvector matrix in which the POD coefficients or modes are in the first column of the matrix, $[\Sigma]$ represents the non-negative diagonal matrix containing the eigenvalues $\sigma_1 \geq \sigma_2 \geq \dots \geq \sigma_M \geq 0$, and $[P]$ denotes the right eigenvector. The most significant ensemble energy content of modes is focused on the POD method to reduce the degree of freedom of the system. The energy level of the system (E_p) which is commonly set as 99 % total energy of the system is defined as [31];

$$E_p = \frac{\sum_{i=1}^N \sigma_i}{\sum_{j=1}^N \sigma_j} \geq \epsilon \quad (7)$$

where N denotes the number of selected eigenvalues such that $N \leq M$. Once the number of eigenvalues N that satisfies Eq. 7 is determined, the snapshot matrix can be reconstructed using the basic functions with the reduced number of design variables by;

$$[\tilde{S}] = [\bar{S}] + \sum_{i=1}^N \alpha_i \varphi_i \text{ or } [\tilde{S}] = [\bar{S}] + [\varphi][\alpha] \quad (8)$$

where \tilde{S} is the reconstructed snapshot matrix, $[\alpha]$ denotes the amplitude matrix that includes α_i . In this study, the POD technique is used for both design variable reduction for the parametric model and the surrogate model.

C. POD-RBF Surrogate Model

POD appears to be a valuable alternative for reduced-order modeling, however, there is no predictive feature for the design exploration process [17]. Therefore, a data fitting technique is implemented to establish a functional relation to explore the design space. In this study, RBF interpolation method is utilized to estimate unknown fields corresponding to the input variables. The mathematical formulation of the RBF can be expressed as;

$$s(x_j) = \sum_{i=1}^n \left(w_i \theta(\|x_j - x_i\|) \right) \quad (9)$$

$$\theta(r) = \sqrt{r^2 + c^2} \quad (10)$$

where $[x]$ is the observation vector with n number of observations, $\|x_j - x_i\|$ is the Euclidean norm calculated for an observation x_j concerning each observation x_i in $[x]$, w_i denote the weights or coefficients of the estimation, θ is the radial basis function, c is a smoothing factor, and r is the Euclidean norm. To use the RBF with accompanying POD, the amplitude matrix $[\alpha]$ can be written as [18, 19];

$$[\alpha] = [B][F] \quad (11)$$

where $[B]$ denotes the coefficient matrix to be computed, and $[F]$ is the interpolation matrix. In Eq. 11, $[\alpha]$, $[B]$, and $[F]$ respectively represent $s(x_j)$, w_i , and $\theta(\|x_j - x_i\|)$ in the RBF defined by Eq. 9. If both sides are multiplied by $[F]^{-1}$ then Eq. 11 is written as;

$$[B] = [\alpha] [F]^{-1} \quad (12)$$

The interpolation matrix $[F]$ for the total number of eigenvalues M is written as;

$$[F] = \begin{bmatrix} \theta(\|x_1 - x_1\|) & \cdots & \theta(\|x_j - x_1\|) & \cdots & \theta(\|x_M - x_1\|) \\ \vdots & \cdots & \vdots & \cdots & \vdots \\ \theta(\|x_1 - x_i\|) & \cdots & \theta(\|x_j - x_i\|) & \cdots & \theta(\|x_M - x_i\|) \\ \vdots & \cdots & \vdots & \cdots & \vdots \\ \theta(\|x_1 - x_M\|) & \cdots & \theta(\|x_j - x_M\|) & \cdots & \theta(\|x_M - x_M\|) \end{bmatrix} \quad (13)$$

The basis functions can be written as;

$$[\hat{\phi}]^T [V] = [B][F] \quad (14)$$

The snapshot matrix can be estimated as;

$$[\tilde{S}] = \bar{S} + [\hat{\phi}][B][F] \quad (15)$$

POD approach can be used as a predictive feature by utilizing the RBF functions. In this study, estimation of design points available in the design space is performed by using this POD-RBF surrogate model.

D. Eigenspace Perturbation Methodology

Turbulence models are constitutive relations attempting to relate quantities of interest to flow parameters using assumptions and simplifications derived from physical intuition and observations. Reynolds-Averaged Navier-Stokes (RANS)-based models that employ a time-averaging process to eliminate temporal dependency are the most affordable and preferable methods for simulating complex engineering flows. RANS modeling is a primary source of epistemic uncertainty for CFD simulations despite their widespread use [21-23]. In this study, the model-form uncertainty originating from the shear stress transport (SST) k - ω turbulence model is determined using the eigenspace perturbation methodology. Eigenspace perturbation methodology is a technique to estimate turbulence model discrepancy using perturbations of eigenvalues and eigenvectors of Reynolds stress tensor that can be expressed as;

$$[R] = 2k \left(\frac{1}{3} [I] + [A] \right) = 2k \left(\frac{1}{3} [I] + [v][\Lambda][v]^T \right) \quad (16)$$

where k denotes the turbulent kinetic energy and $[I]$ is the second-order identity tensor. The anisotropy tensor denoted by $[A]$ is decomposed to $[v]$ and $[\Lambda]$, which are the eigenvector matrix and the diagonal matrix of eigenvalues $\lambda_1, \lambda_2, \lambda_3$ of the anisotropy tensor of the Reynolds stress, respectively. In this study, only the perturbations of the eigenvalues and eigenvectors are considered to introduce the model form uncertainty [21-23], and the perturbed Reynolds stress is defined as;

$$[R] = 2k^* \left(\frac{1}{3} [I] + [v^*][\Lambda^*][v^*]^T \right) \quad (17)$$

By perturbing them to their limiting states, the maximum information can be obtained for the uncertainty estimation. For this purpose, five different extremal states of the Reynolds tensor are calculated using the eigenspace perturbation methodology. These five extremal states involve the combination of three extremal states for the eigenvalues and two extremal alignments of the eigenvectors. Five distinct simulations (three simulations for eigenvalues perturbation and two simulations for eigenvectors perturbation) are performed to quantify the uncertainty bounds.

The flowchart of the eigenspace perturbation methodology to include the model-form uncertainty is depicted in Fig. 1. To implement this methodology, first, the simulation conditions such as the boundary, initial conditions, flux splitting method, etc. are defined. The unperturbed Reynolds stress tensor for each node of the computational grid is calculated based on these simulation conditions. Then, the eigenspace perturbation is utilized and the perturbed Reynolds stress tensor required for turbulent and convective flux computations is calculated. The new perturbed fluxes are then used to march the solution forward in pseudo time. As the solution converges, the Reynolds stress tensor also converges to its perturbed state. The five distinct simulations are performed using this method in Fig. 1 and the uncertainty bounds are determined concerning the unperturbed state.

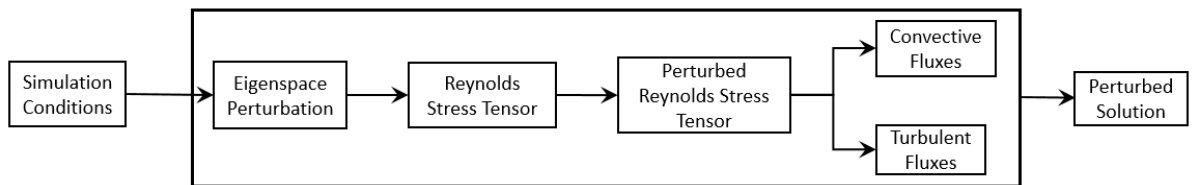


Fig. 1 The flowchart of the uncertainty quantification process

E. Inductive Design Exploration Method

Inductive Design Exploration Method (IDEM) is a top-down robust optimization technique to obtain the design alternatives available in the design space that satisfy the design requirements taking uncertainties into account [24]. The main idea of the IDEM is to determine Hyper Dimensional Error Metric Index (HD-EMI) finding the minimum distance between the response of a design alternative and the boundary of the design requirements. The schematic representation of the IDEM computations is given in Fig. 2.

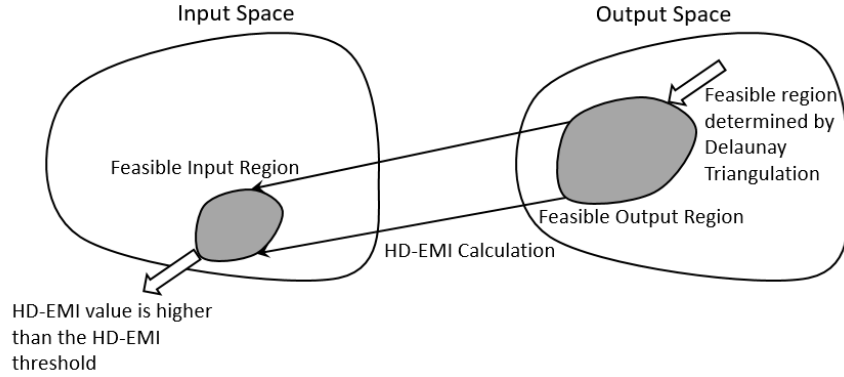


Fig. 2. The schematic of the IDEM procedure

As it is seen from Fig. 2, the design space is divided into two different groups as input and output space. A boundary determined by using Delaunay triangulation is generated corresponding to the design requirements [32]. HD-EMI value of each design alternatives is computed considering uncertainties. The feasible solutions are selected with the HD-EMI value that is higher than the predefined HD-EMI threshold. It is obvious that the HD-EMI value which is a selection criterion has vital importance to obtain robust solutions. It is defined as the ratio of the minimum distance between the output value and the design requirement boundary, and the distance between the output value and the uncertainty bound. HD-EMI value has negative unity when the solution is not feasible. The schematic representation and mathematical definition of the HD-EMI value calculation are represented in Fig. 3 and Eq. 18 respectively.

$$HD_{EMI} = \begin{cases} \min_i \frac{\|\bar{y} - B_{j,i}\|}{\Delta y_i}, \\ -1, \end{cases} \quad (18)$$

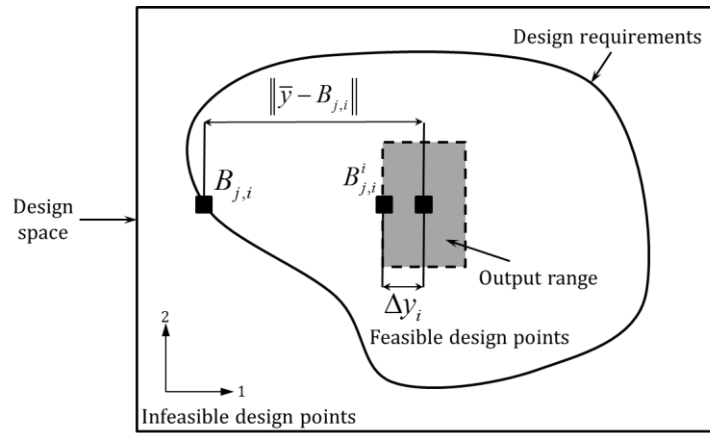


Fig. 3 The schematic of the HD-EMI calculation

where i and j represent the output dimension Δy_i denotes the distance between the mean of the output range and the maximum or minimum value of the output range considering uncertainty. $\|\bar{y} - B_{j,i}\|$ is the distance between the boundary $B_{j,i}$ computed by the performance requirements and the mean of the output range denoted by \bar{y} .

F. Proposed POD-based IDEM Framework

Robust solutions available in the design space are obtained by considering model-form uncertainties by the IDEM procedure. Firstly, the number of design variables required for the wing geometry parametrization is reduced with the POD technique. The parametric model is reconstructed using the POD coefficients that satisfy 99 % of the total energy of the system. The computational cost due to the CFD analyses required for the design exploration is reduced with the POD-RBF based surrogate model. The model-form uncertainties are determined with the eigenspace perturbation methodology explained in Section III-D. The robust solutions that satisfy the design requirements are obtained with the IDEM procedure. The proposed IDEM optimization framework is illustrated in Fig. 4.

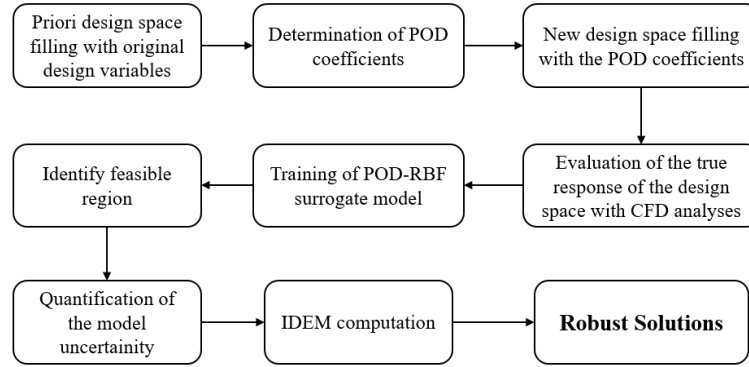


Fig. 4 The proposed IDEM robust optimization framework

- i. Prior design space is generated with the initial design variables to develop the snapshot matrix. 15 various design alternatives for each design variables ($15 \times M$) are sampled using Latin Hypercube Sampling (LHS) which is a random sample method [33].
- ii. The dominant features that satisfy 99 % of the total energy of the snapshot matrix are extracted with Singular Value Decomposition (SVD) explained in Section III-B.
- iii. The geometry is reparametrized with the POD coefficients and the design space using the generated reduced-order model. New design space-filling by the LHS method is employed with $15 \times N$ and the true responses of the design points are evaluated with the CFD analyses.
- iv. The POD-RBF based surrogate model explained in Section III-C is constructed to enrich the design space using the sampled points.
- v. The POD coefficients and estimated output are separately stored as the input and output database.
- vi. The performance requirements available in the design space are identified and the boundary for the performance requirements is specified with the Delaunay triangulation.
- vii. The model-form uncertainties are determined with the eigenspace perturbation methodology explained in Section III-D for each design objective and conditions.
- viii. HD-EMI threshold is set as unity to determine the robustness level of each design alternatives [25].
- ix. Robust solutions considering the uncertainties are obtained and listed following the HD-EMI and design objective function values using IDEM described in Section III-E.

IV. Results and Discussion

A. Problem Definition of the Aircraft Wing Design Optimization

In this section, the design objectives and conditions of an aircraft wing design optimization problem are described. Three design objectives are aimed to be improved with the design optimization of the wing:

- (1) Rolling moment coefficient gradient ($CR-\beta$),
- (2) Lift coefficient (CL),
- (3) Drag coefficient (CD).

Each of these three design objectives is evaluated for a different case of flow conditions listed in Table 1. There are three different cases of flow conditions considered in this study:

Case 1: Mach number is 0.186, the angle of attack (AOA) is 8 degrees and the side-slip angle (β) is 10 degrees at the sea level [34].

In the first case, the design objective $CR-\beta$ is selected to satisfy the approach scenario of an aircraft extracting flap configuration at sea-level altitude. Therefore, lateral stability parameter $CR-\beta$ is intended to be reduced as much as possible [34].

Case 2: Mach number is 0.4, AOA is 10 degrees, and β is 0° [34]. The objective is to improve the loop-maneuvering entrance at 3048 m (10,000 ft) pressure altitude for the flow conditions of this second case. These flow conditions are considered for the case without the side wind condition.

In the second case, the design objective CL is aimed to be maximized. The increase of CL will directly improve the loop maneuvering entrance [34].

Case 3: Mach number is 0.53, AOA is -1 degree and β is 0 degree at sea level. Mach number without side wind condition is selected following [34].

In the third case, the CD should be minimized while the CL should be maximized to improve the high-speed characteristic of the aircraft. To achieve these objectives, the ratio CD/CL is defined to be reduced as much as possible at sea-level altitude [35].

Table 1 Design objectives and flow conditions

<i>Evaluating (Design Objectives) :</i>
Case-1: Minimize $CR-\beta$
Case-2: Maximize CL
Case-3: Minimize CD/CL
<i>Flow Conditions :</i>
Case-1 : 0.18 Mach, 8 AOA, 10 BETA, Sea-level
Case-2 : 0.4 Mach, 10 AOA, 0 BETA, 3048 m (10,000) ft
Case-3 : 0.53 Mach, -1 AOA, 0 BETA, Sea-level

B. Geometry Parametrization

The wing geometry model is composed of two airfoil sections which are located at the root and tip section. NACA 63415 airfoil type is used as the initial geometry for both root and tip airfoil sections. Each airfoil geometry is modeled to consist of the upper and lower curve of the airfoil. Bezier curves explained in Section III-A are used to parametrize the airfoil geometries and the 5th order Bezier curve is used for each part of the airfoil shapes. There is no change in the location of the leading and trailing edge of the airfoil sections. Only the location of the control points available in the middle part of the airfoil geometries seen in Fig. 5 is varied for the design exploration process. Therefore, 32 design variables which are X and Z location of the control points are required to identify the airfoil sections.

In addition to the Bezier control points that define the airfoil shapes of the wing, five additional design variables shown in Fig. 6, are defined to model the wing geometry. As a result of the parametrization process, 37 design variables are required to define the wing geometry. The design limits for the design exploration are given in Table 2.

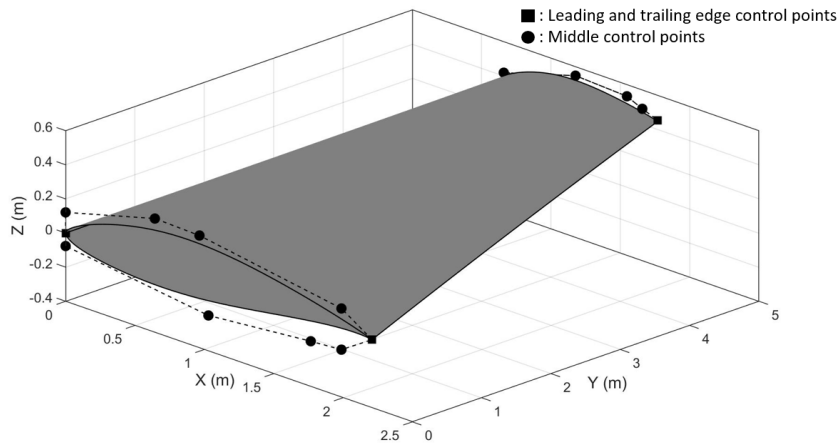


Fig. 5 Initial wing geometry generated using Bezier surfaces

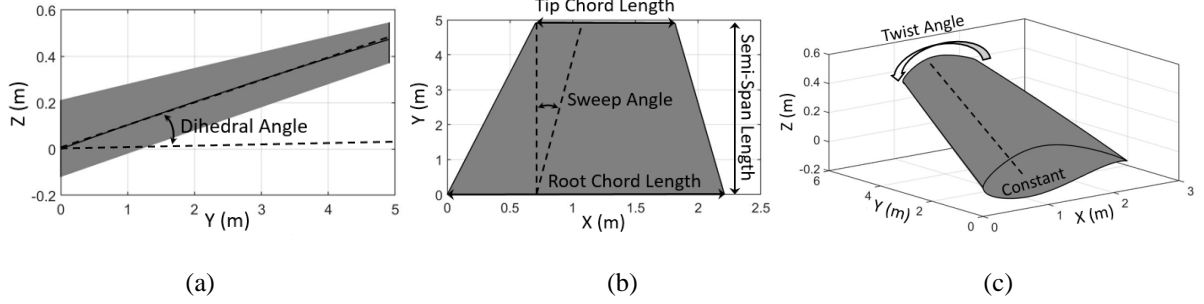


Fig. 6 Definition of the 3D wing parameters (a) Front view (YZ view) (b) Top view (XY view) (c) Isometric View

The initial wing geometry is generated to be used for the optimization process. First, the initial root and tip airfoils are selected as NACA 63415 laminar type airfoil and three-dimensional wing parameters are shown in Table 2. The upper and lower limit of the airfoil are depicted in Fig. 7

Table 2 Upper and lower limit of wing design parameters

Parameter	Initial values	Lower limit	Upper limit
Wing Area (m^2)	16.2	16.2	16.2
Aspect Ratio	5.75	4.5	7.5
Taper Ratio	0.45	0.35	0.75
Sweep Angle (deg)	5	4	12
Dihedral Angle (deg)	5	2	8
Twist Angle (deg)	-1.5	0	-4

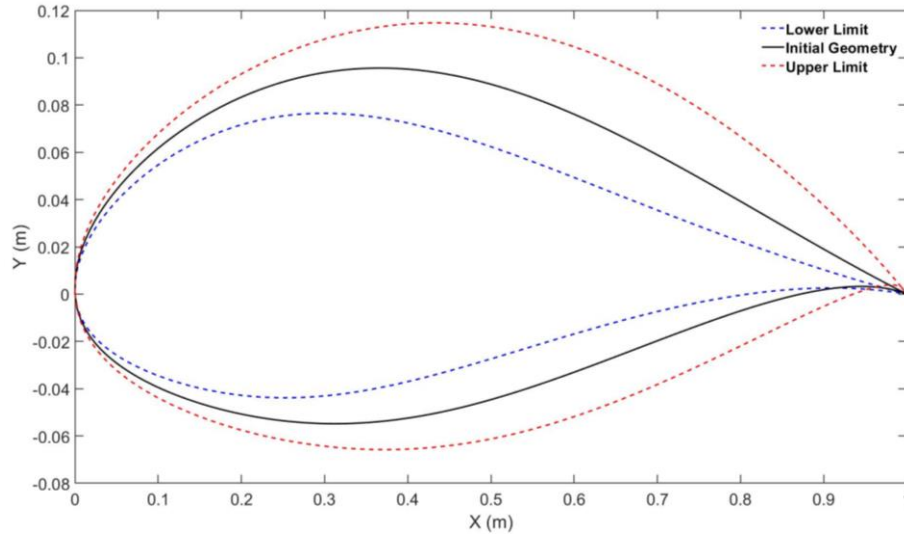


Fig. 7 The upper and lower limit of the root and tip airfoil profile

C. Reduction of Design Variables by POD

The number of the design variables has a significant impact on the computational time required for the design exploration, thus, the data reduction procedure explained in Section III -B is applied. Prior design space is generated with the original number of design parameters ($M=37$). Latin Hypercube Sampling (LHS) is employed to randomly generate the discrete points available in the design space within the design limits explained in Section IV-B. $M \times 15$ different wing geometries are used to construct the snapshot matrix explained in Section III-B. Dominant features of the design space are extracted using POD. The number of design variables is reduced to dominant ensemble POD coefficients (N) which satisfy 99 % of the total energy content of the design space. The energy content change with the number of dominant modes is given in Fig. 8.

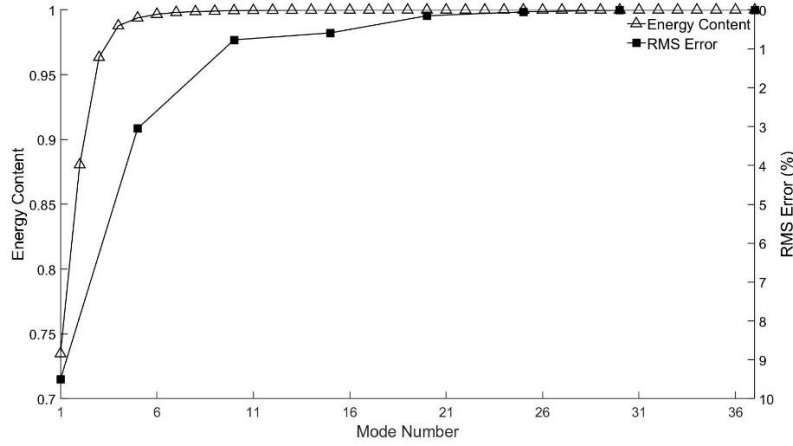


Fig. 8 The energy content and RMS error results with the change of the number of modes

As it can be seen from Fig. 8, 99 % of the total energy content of the flow is represented after the first 5 modes. As a result of POD, the number of design variables required for geometry parametrization is reduced from $M=37$ to $N=5$. Design exploration is performed using 5 POD coefficients to obtain the new wing geometry. The comparison between the original geometry and the geometry reconstructed with 5 POD coefficients is shown in Fig. 9.

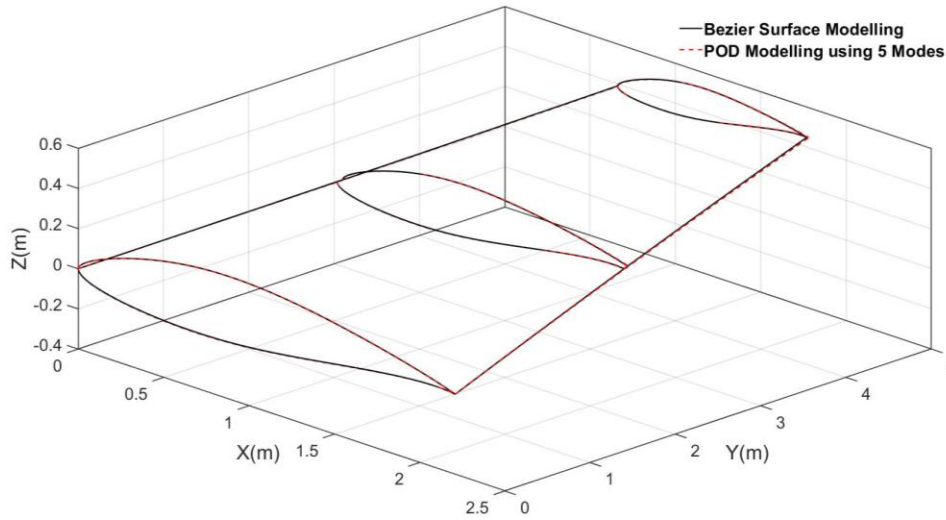


Fig. 9 Geometric comparison of the original Bezier surface model and the model obtained with POD

It is seen from the geometry comparisons, there is almost no difference compared to the original geometry. Then, to reduce the number of variables, 5 modes can be accepted as suitable for the optimization process. The dominant POD coefficients are used to parametrize the wing geometry to obtain different wing alternatives. The number of design variables in the optimization is reduced from 37 to 5. Thus, POD coefficients become the new design variables. Within the shape optimization framework, the LHS is applied to the POD coefficients to obtain the alternative samples of the geometry. The bounds of the POD coefficients used in the LHS method are listed in Table A-1.

D. Design Conditions and Grid Independency Study

CFD analyses are performed to evaluate the true response of the discrete points available in the design space. Before performing design exploration, a grid independency study is conducted to reduce the computational cost concern with maintaining the numerical accuracy. Four different computational grids given in Fig. 10 are used for the mesh independency study. The number of grid points increases from the computational grid 1 to 4. The computational grid properties and estimated computational time required for the design space generation are given in Table 3.

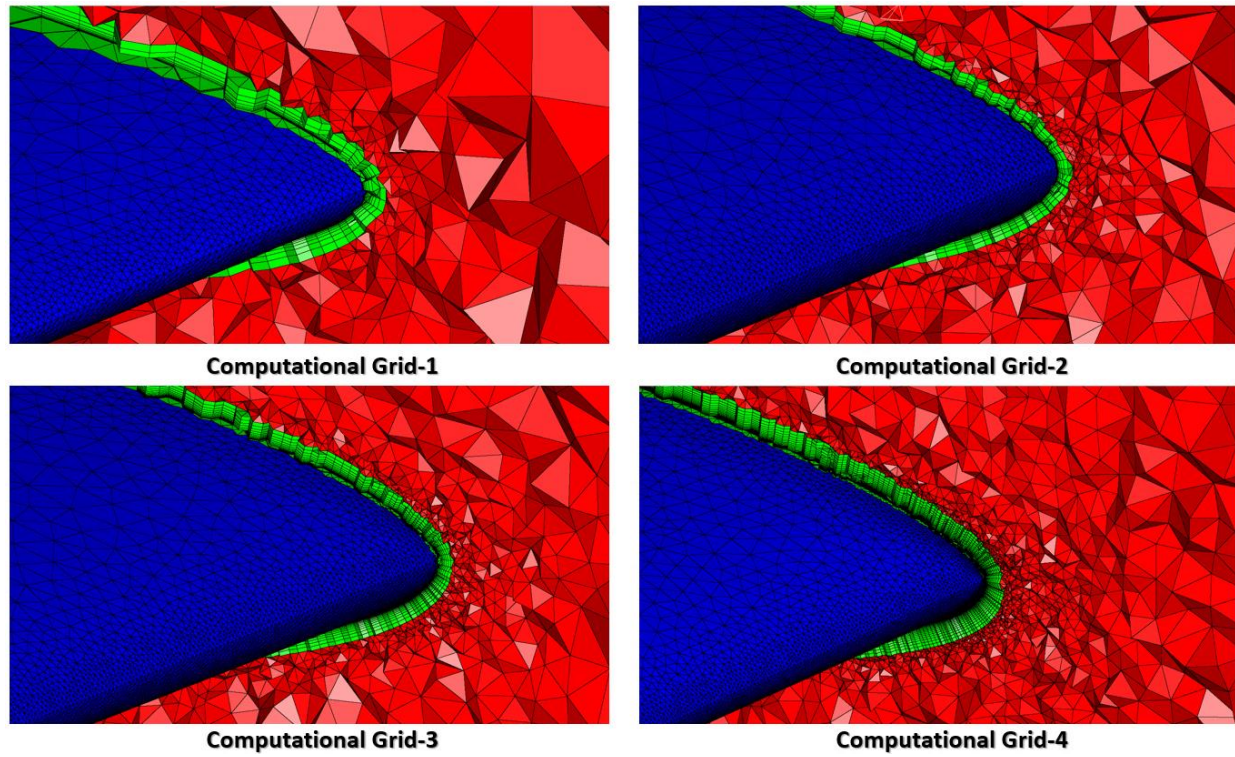


Fig. 10 Computational grids for grid independency study

Table 3 Grid and computational time requirements for design space generation

Computational grid	Minimum cell height (mm)	Number of prismatic elements	Total number of elements	Computational time required for design space generation
Grid-1	0.0027	19	1,634,260	195 hours
Grid-2	0.002	22	3,974,336	475 hours
Grid-3	0.0012	35	8,802,914	1073 hours
Grid-4	0.00027	69	22,395,015	2675 hours

The CFD analyses for the initial geometry explained in Section IV-B are performed using a reliable open-source solver SU2 which is based on the Finite Volume Methodology (FVM) [36]. Steady-state simulations are performed for Reynolds numbers of 8.9 million, 21.1 million, and 24.6 million for the computational cases given in Table 1 (Case 1, Case 2, and Case 3), respectively. SST $k-\omega$ turbulence model, which is accurate for the separation prediction caused by the inverse pressure gradient and combines the advantages of the standard $k-\omega$ and standard $k-\epsilon$ turbulence models, is used in the CFD analyses [46]. The design objectives explained in Section IV-A obtained from the CFD analyses are compared and the percentage differences are calculated for each computational grid concerning the finest computational grid (Computational grid-4).

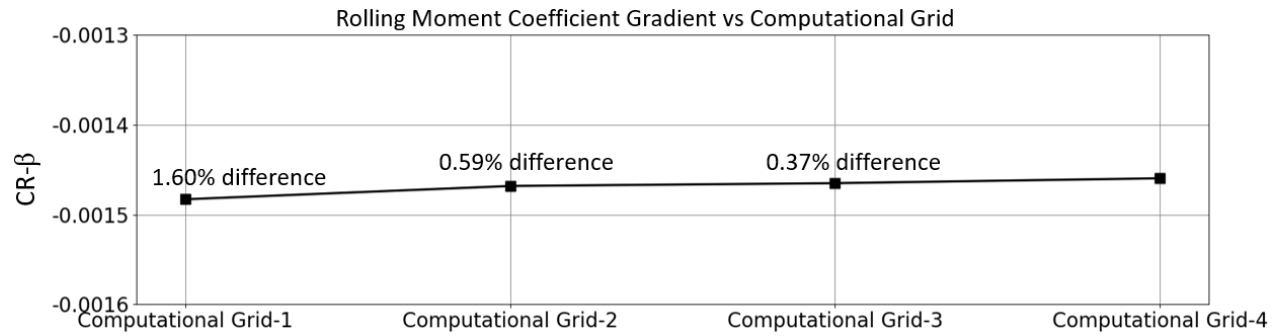


Fig. 11 Rolling moment coefficient gradients and drag count comparison for the conditions of Case-1

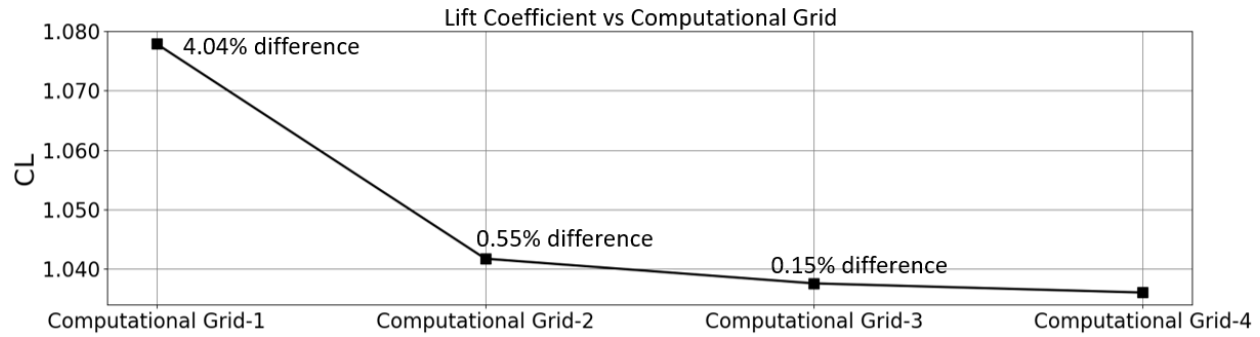


Fig. 12 Lift coefficients and drag count comparison for the conditions of Case-2

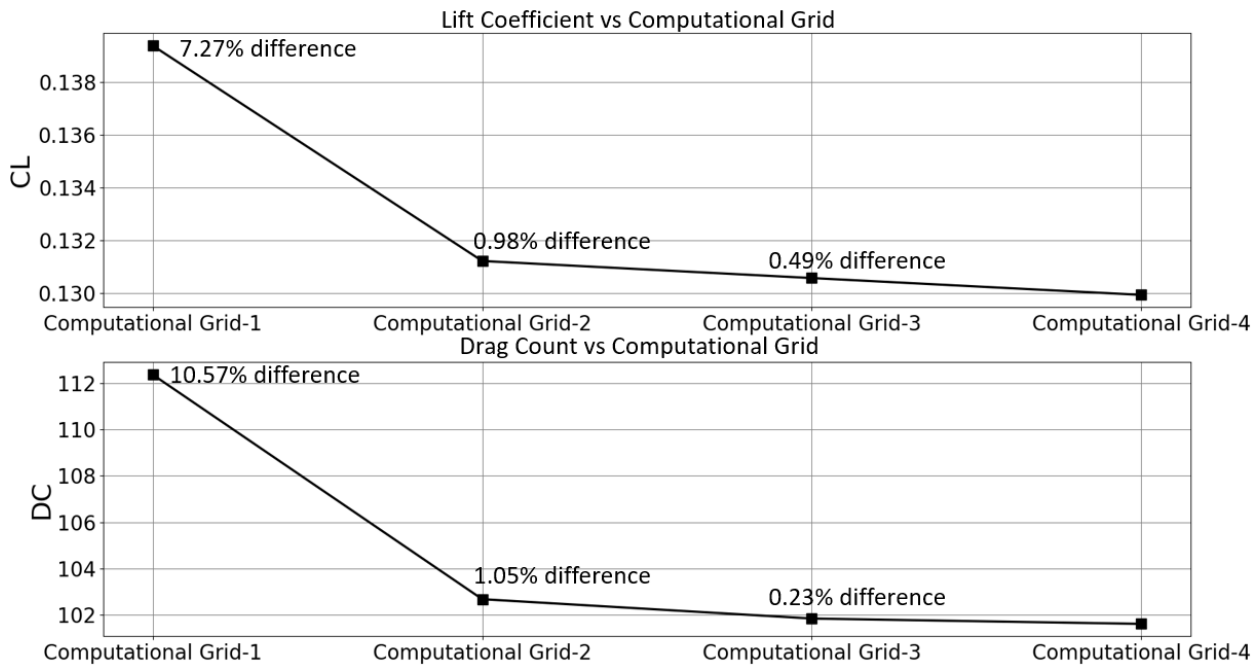


Fig. 13 Lift coefficients and drag count comparison for the conditions of Case-3

As it can be clearly seen from the figures, the computational grid-2 is the most suitable grid under the consideration of computational cost and accuracy. The most discrepancy (1.05 %) compared to computational grid-4 is observed in the drag count value for Case-3. To visualize the grid independency results, pressure coefficient for computational grid-2 and 4 are given side to side for comparison in Fig. 14-16 for Case-1, Case-2, and Case-3, respectively.

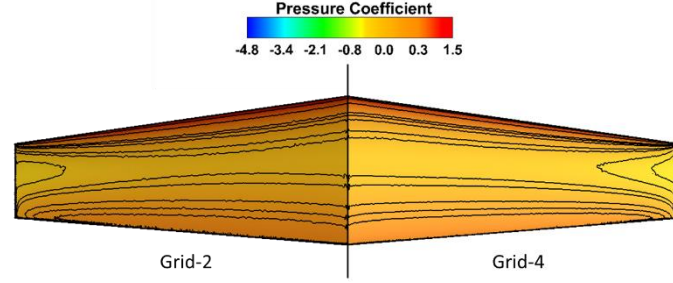


Fig. 14 Pressure contours and streamlines for Case-1 with computational grid-2 and computational grid-4

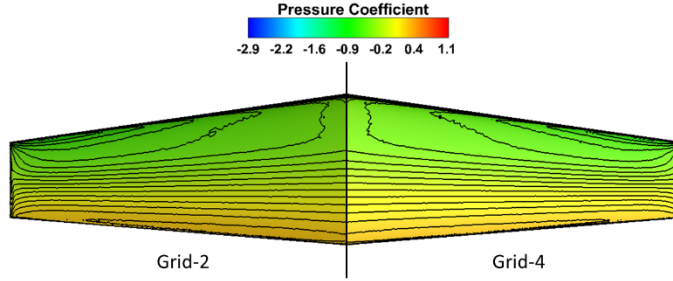


Fig. 15 Pressure contours and streamlines for Case-2 with computational grid-2 and computational grid-4

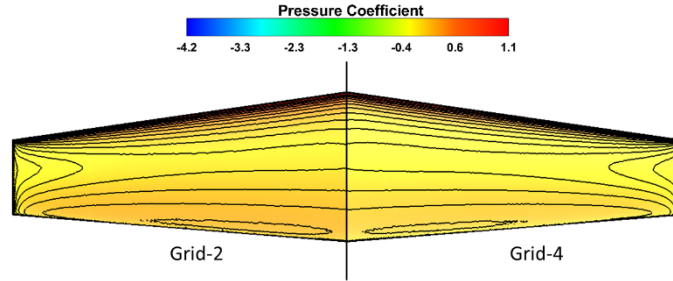


Fig. 16 Pressure contours and streamlines for Case-2 with computational grid-2 and computational grid-4

Pressure contours on the wings show that Grid-2 has an acceptable agreement with the fine grid defined as Grid-4. Hence, it is concluded that Grid-2 is suitable for further CFD analyses.

E. Response Surface Modeling by POD-RBF

The discrete points required for the design space generation corresponding to the first 5 dominant POD coefficients are sampled using the LHS. 15 discrete points are sampled for each POD coefficients, total 75 discrete points are analyzed to evaluate the true response following the conditions given in Table 1. The unknown points available in the design space are derived with the POD-RBF surrogate model. Before the design exploration process, the POD-RBF surrogate model is validated with the new validation points. 20 % number of total discrete points is generated and the estimated and CFD analyses results comparison with the adjusted-R square error metric in Table 4 [41]. The POD-RBF surrogate model is also compared with DAKOTA, which is a reliable open-source optimization tool [43].

Table 4 Comparison of adjusted R-square with 5 POD coefficients between POD-RBF and DAKOTA

Method	0.18 M CR	0.4 M CL	0.53 M CL	0.53 M CD
POD-RBF	0.999	0.999	0.997	0.991
Dakota RBF	0.999	0.999	0.991	0.985

According to Table 4, the estimated results are in very good agreement with the analysis results. The largest deviation (the last column of the table that is 0.991) is observed in the drag coefficient estimation for Case-3. However, the difference is acceptable. It is also observed that the in-house developed POD-RBF code gives more accurate results compared to the DAKOTA RBF algorithm. In the light of these results, it is concluded that POD-RBF is an effective surrogate modeling technique and 5000 additional discrete points are estimated using the POD-RBF surrogate model.

F. Introduction of Model Uncertainty

The model-form uncertainty is determined using the eigenspace perturbation methodology explained in Section III-D. Five distinct CFD analyses for each design point (Case-1, 2, and 3) are performed with both perturbed eigenvalues and eigenvectors of the Reynolds stress tensor, then the uncertainty due to turbulence is computed from the difference between the perturbed solutions and the unperturbed solution. The lower and upper bound of the uncertainty limit is given in Table 5.

Table 5 Uncertainty limits between the perturbed and unperturbed solutions

Uncertainty Limit	$CR-\beta$ @Case-1	CL @Case-2	CL @Case-3	DC @Case-3
Lower bound of perturbed CFD result	-0.001467	1.045	0.133	91.94
Unperturbed CFD result	-0.001468	1.048	0.131	102.68
Upper bound of perturbed CFD result	-0.001461	1.065	0.138	115.73

As it can be seen from Table 5, the lower bound of the uncertainty limit for $CR-\beta$ for Case-1 (first column of the table) and CL for Case-3 (third column of the table) is higher than the unperturbed solution. There is no potential result, which is lower than the unperturbed solution for these design objectives. However, CL for Case-2 and DC for Case-3 can have a lower value compared to the unperturbed solution. The uncertainty limit of the design objectives is given in Fig. 17-19.

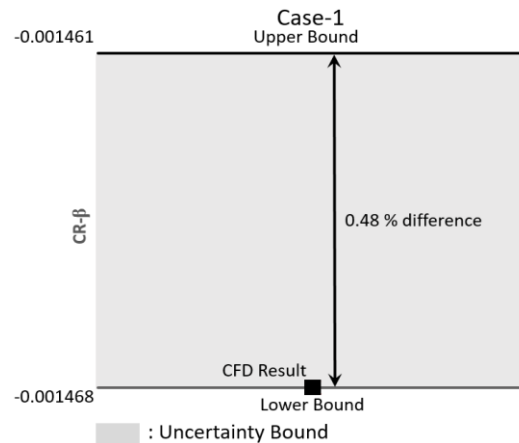


Fig. 17 Uncertainty bound for rolling moment coefficient for Case-1

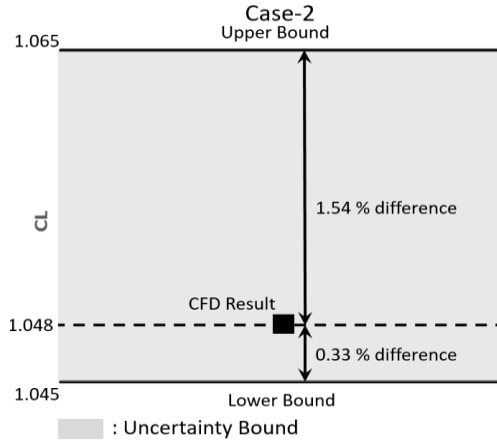


Fig. 18 Uncertainty bound for lift coefficient for Case-2

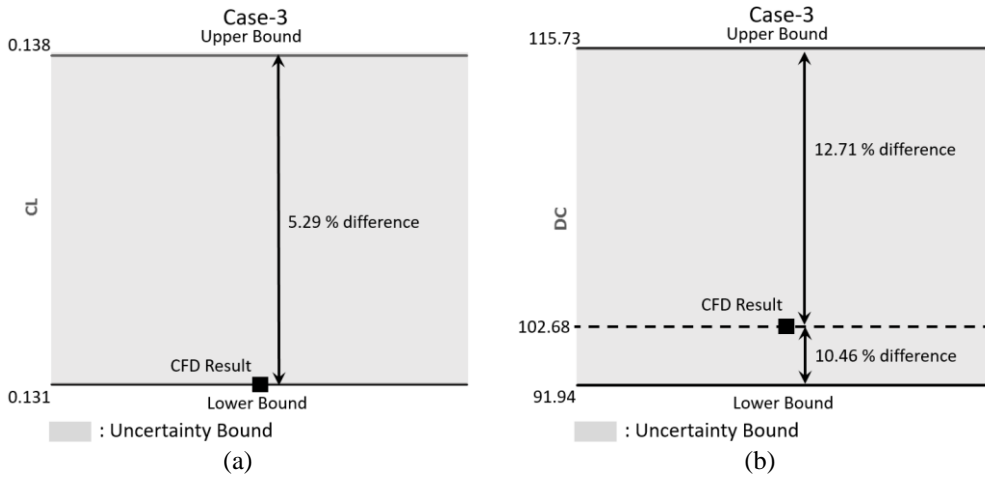


Fig. 19 Uncertainty bound (a) lift coefficient (b) drag count for Case-3

In this study, uncertainty estimations given in Fig. 17-19 are implemented for robust optimization computation.

G. Application of IDEM for Aircraft Wing Design

The open-source Python code for IDEM, called pyDEM [32] is modified to include the POD-RBF surrogate modeling capability and the model-form uncertainties obtained by the eigenspace perturbation method. To verify the effectiveness of the modified pyDEM code, it is implemented to the wing shape design exploration benchmark case. According to [44], 4123 discrete design points are used for the IDEM robust optimization process. To have a similar design point number, in this study, 5000 additional design points are generated to be available in the design space given in Table A-1 which are different from the training data derived using LHS. The POD-RBF data prediction algorithm evaluates the responses of the design points. IDEM searches the robust solutions from the design points.

G.1. Wing shape design exploration benchmark case

In this section, the robust solutions are determined with IDEM computations for the design space explained in Section IV-B under the consideration of the design constraints given in Table 6. The modified pyDEM code that the POD-RBF surrogate model and model-form uncertainties are implemented is used for IDEM computations. There are three different design objectives, which are minimizing $CR-\beta$ and CD/CL for Case-1 and Case-3 respectively, and maximizing CL for Case-2. The maximization objective of CL can be identified to the optimization as the minimization of $1/CL$. Since there are multiple objectives to be minimized simultaneously, for the sake of proper objective function minimization, the objective functions are normalized to the same order to eliminate the errors due to the different scales of the objective functions [45, 46]. The normalization process of the i -th objective function is given as;

$$F_i^* = \frac{F_i(x) - F_i^{\min}}{F_i^{\max} - F_i^{\min}} \quad (19)$$

where F_i^* denotes the normalized objective function, $F_i(x)$ is the original objective function, F_i^{\max} and F_i^{\min} are the maximum and minimum response available in the design space, respectively. A single-level optimization with the summation of multiple objectives multiplied by some weights w_i is employed in this study. In addition, the objective functions should be greater than some minimum values. The minimum rolling moment ($CR-\beta_{min}$) for Case-1 and lift coefficient (CL_{min}) for Case-2 are identified as -0.0004363 per degree and 1.05 respectively in correspondence with [34]. The conditions, constraints, uncertainties, and design objectives are summarized in Table 6.

Table 6 Mathematical form of robust optimization

Design Space :
POD coefficients as design variables
Response :
Optimized POD coefficients constructing robust wing design alternatives
Constraints :
CR- β @Case-1 \leq -0.0004363 per degrees
CL@ Case-2 \geq 1.05
CL@ Case-3 \geq 0.1
Uncertainty :
CR- β @0.18 M (%) = [0,0.48]
CL@0.4 M (%) = [0.33,1.54]
CL@0.53 M (%) = [0,5.29]
CD@0.53 M (%) = [10.46,12.71]
Minimize :
$Z = w_1(F_{CR-\beta@Case-1}^*) + w_2(F_{CL@Case-2}^*) + w_3(F_{CD/CL@Case-3}^*)$
$w_1, w_2 = 0.33, w_3 = 0.34$

G.2. Results of IDEM with 5 POD coefficients

617 robust design alternatives that the design requirements given in Table 6 are satisfied and the model-form uncertainties given in Table 5 are considered are obtained with the IDEM computations. The properties of the first three robust design alternatives with the lowest objective function value and the highest robustness level, in order words, the highest HD-EMI value are given in Table 7.

Table 7 Results of three robust design configurations with minimum objective function and maximum HD-EMI values for 5 POD coefficients

Configuration	Taper Ratio	Aspect Ratio	Dihedral Angle (deg)	Sweep Angle (deg)	Twist Angle (deg)	Objective Function	HD-EMI
Initial	0.50	5.91	5.00	5.00	-1.50	0.546	0.743
Robust Solutions with minimum objective function values							
1	0.41	7.01	4.05	8.52	-1.39	0.340	1.084
2	0.56	6.49	4.61	8.81	-1.76	0.345	1.015
3	0.44	6.77	4.63	8.43	-1.50	0.346	1.169
Robust solutions with maximum HD-EMI values							
4	0.46	5.89	5.17	5.50	-1.67	0.530	1.275
5	0.44	6.29	5.85	6.17	-1.66	0.524	1.273
6	0.47	5.99	5.42	5.41	-1.70	0.468	1.271

It is seen from Table 7 that, the taper ratio of the robust solutions is less than the initial configuration except for the configuration-2. This geometric difference can be seen from the ratio from the tip chord length to the root chord length given in Fig. 20 (a) and (b). On the contrary, the aspect ratio of all robust solutions except for configuration-4 is higher than that of the initial configuration. Similarly, this difference can be seen from the semi-span length Fig. 20 (a) and (b). The semi-span length of the robust solutions is higher than the initial geometry. The sweep angle of all robust solutions is higher than the initial configuration and it is seen in Fig. 20 (a) and (b). The dihedral angle of the first three solutions is smaller and the last three solutions are higher than the initial geometry seen in Fig. 20 (e) and (f). The twist angle of the robust solutions except for configuration-1 and 3 is larger than the initial configuration seen

in Fig. 20 (c) and (d). All objective function values are lower than the initial configuration as it is expected due to the sake of the optimization process. Configuration-4, which has the highest HD-EMI value, is the most robust solution among all robust solution alternatives given in Table 7. However, this solution has the highest objective function value. The last three configurations that are the first three robust solutions with the highest HD-EMI value have a larger objective function value compared to the first three configurations. It is observed that increasing the robustness level of a solution cause increasing the objective function value.

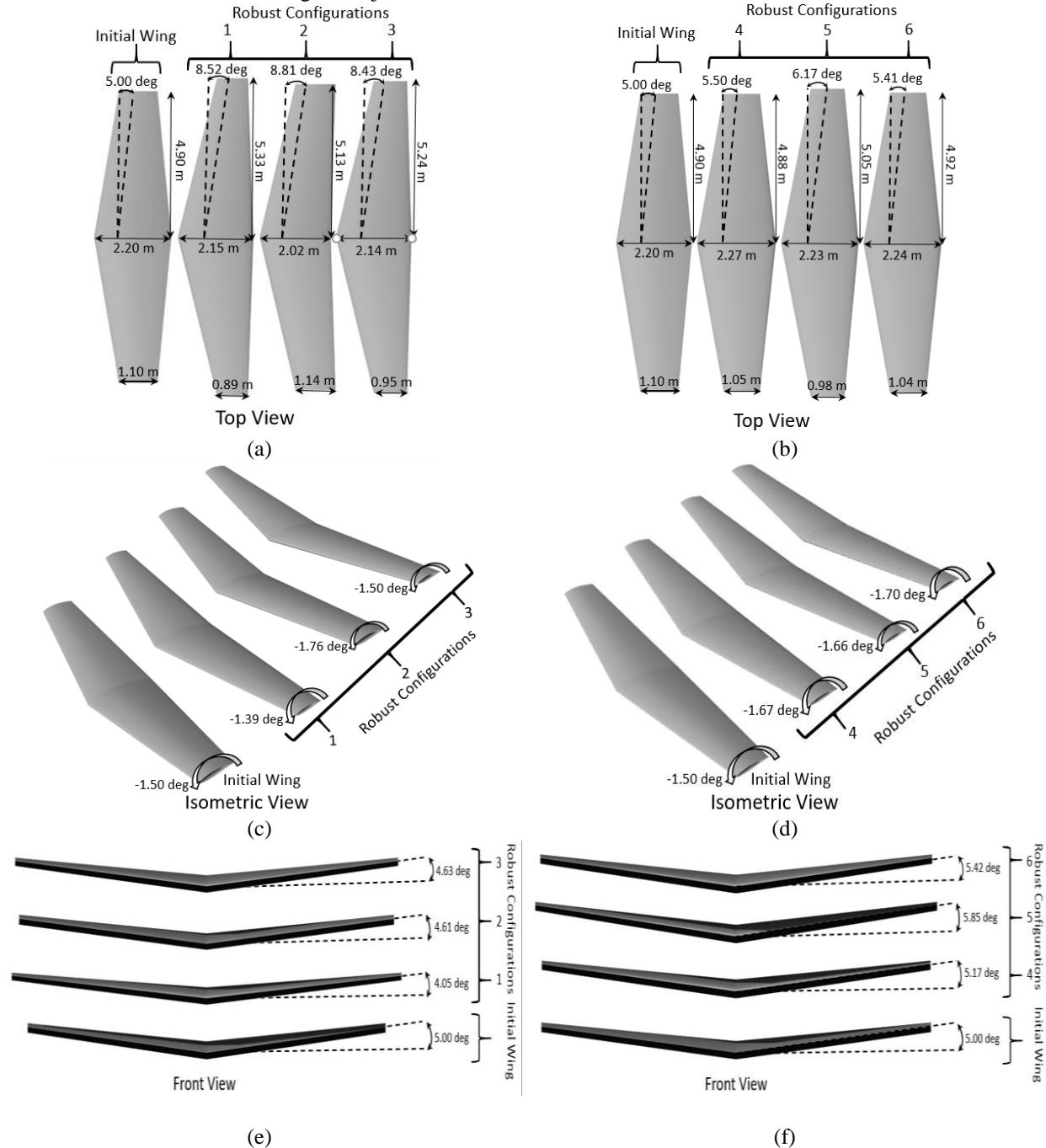


Fig. 20 Robust solutions obtained by 5 POD for the lowest objective function values (a) Top view (c) Isometric view (e) Front view and 5 POD for the highest HD-EMI values (b) Top view (d) Isometric view (f) Front view

The tip and root airfoil sections of the robust solutions are given in Fig. 21. The maximum thickness of the root airfoil is not changed dramatically. The largest geometric discrepancy is observed near the trailing edge location seen

in Fig. 21 for the root airfoil section. For the tip airfoil section of the robust solutions, there is a significant change seen in Fig. 21 in terms of the whole airfoil shape. The largest discrepancy is observed for configuration-2.

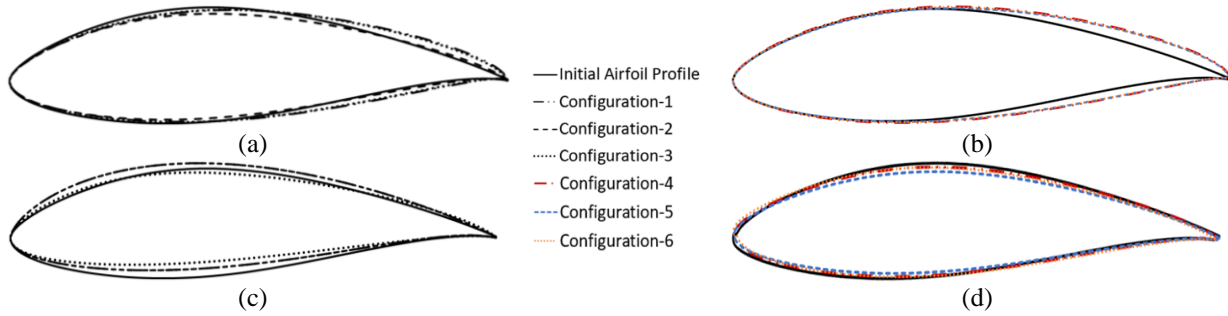


Fig. 21 Robust airfoil profiles (a) root and (b) tip airfoil profiles for 5 POD (c) root and (d) tip airfoil profiles for 25 POD coefficients

G.3. Validation of optimized solutions with CFD simulations

CFD analyses are performed to validate the robust solution estimations with the POD-RBF based IDEM computations. The CFD results or the true response of the robust solutions and estimated values with the design conditions stated in Table 1 (Case-1, Case-2, and Case-3) are compared with the Mean Absolute Error (MAE) metric in Table 8.

Table 8 MAE results between the estimated values and CFD results			
<i>5 POD Coefficients-Minimum Objective Function Values</i>		MAE (%)	
<i>Configuration</i>	<i>CR-β@ Case-1</i>	<i>CL@ Case-2</i>	<i>CD/CL@ Case-3</i>
Design-1	0.49	1.50	0.82
Design-2	0.90	1.33	0.77
Design-3	1.71	1.97	1.60
<i>5 POD Coefficients-Maximum Robustness Level</i>		MAE (%)	
Design-4	2.18	2.79	1.39
Design-5	1.02	2.61	2.58
Design-6	0.44	1.50	1.60

It is seen from Table 8, the first three robust solutions that have the lowest objective value available in the design space have the MAE under 2 %. The maximum MAE is observed as 1.97 % in design-3 for Case-2. (the third row and second column of Table 8) The robust solutions, which have the highest robustness level (Design-4, 5, and 6) have higher MAE value compared to the first three configurations. However, the maximum MAE results are observed as 2.79 % in the design-4 for the Case-2 (the fourth row and second column of the table) Since the MAE results are under the value of 3 % for the robust solutions, it is accepted that the estimated results are appropriate with the true response obtained by the CFD analyses.

V. Conclusion

In this study, a multi-objective robust shape optimization approach is implemented for the design of an aircraft wing. In this approach, the number of design variables required for the wing geometry parametrization is reduced using POD. The robust solutions considering model-form uncertainties are obtained with the POD-RBF based IDEM framework. In the first step, an initial wing geometry is parametrized with 37 design variables. Then, the dominant features of the shape are extracted and the POD coefficients that satisfy the 99 % of the total energy content of the system are determined. It is decided that the first five POD coefficients are sufficient to reconstruct the wing geometry and these coefficients are accepted as the new design variables.

Since POD provides a low-order approximation, it is used as a surrogate model accompanying with RBF to estimate the unknown field available in the design space. Validation of the data-fitting method is conducted with new 20 % of the sampled points available in the design space. The estimated and true responses obtained by the CFD

analyses are compared with each other using the adjusted r-square error metric. The validation points are also determined with a reliable open-source optimization tool DAKOTA. The estimated results are highly compatible with the CFD results as well as DAKOTA results. Therefore, it is accepted that the developed POD-RBF surrogate model can be used for the optimization process.

The model-form uncertainties originating from the turbulence model are introduced to the model using the eigenspace perturbation methodology for each design objective. Five distinct simulations are performed (three of them for the eigenvalue and two of them for the eigenvector perturbation) to observe the deviation of the results compared to the unperturbed solution. The lower and upper bound of the uncertainty limit are determined to be used for the robust optimization computations.

The robust solutions are acquired by IDEM computations and put in an order starting from the one that gives the most minimum objective function value and maximum robustness level (i.e. the highest HD-EMI value). Three candidate robust design alternatives are selected for each criterion and compared with the initial wing geometry for both the design space with 5 POD coefficients. The results showed that the design space generation with 5 POD coefficients can essentially reduce the computational time, which is required for the evaluation of the true response of the design alternatives with CFD analyses. Furthermore, the comparisons with actual CFD analysis results have good accuracy when 5 POD coefficients were used. Identifying the POD coefficients based on the energy content and constructing the design space with a smaller number of POD coefficients is found to be a suitable approach for the limited computational time and/or resources. It is concluded that the improved IDEM with POD is an effective design exploration tool that can be used in the aerodynamic field to find optimal design range for specified performance conditions. Future work includes the consideration of the input uncertainties in the optimization to have a rigorous design evaluation.

VI. Acknowledge

This research did not receive any specific grant from funding agencies in the public, commercial, or not-for-profit sectors.

VII. Appendix

A. Design limits of 5 POD coefficients

Design space exploration for the design space constructed using 5 POD coefficients is achieved with the limits given in Table A-1.

Table A-1 Design limits for the design space constructed by 5 POD coefficients

Design Space	Lower Bound	Initial Wing Geometry	Upper Bound
POD Coefficient-1	-2.015661	-0.201566	2.015661
POD Coefficient-2	-1.021244	-0.928403	1.021244
POD Coefficient-3	-0.773974	-0.019349	0.773974
POD Coefficient-4	-0.747255	0.106751	0.747255
POD Coefficient-5	-0.308858	0.000515	0.308858

References

- 1 Castonguay P., Nadarajah S., Effect of Shape Parametrization on Aerodynamic Shape Optimization, AIAA Aerospace Sciences, January 2017. <https://doi.org/10.2514/6.2007-59>
- 2 Sripawadkul V., Padulo M., Guenov M., A Comparison of Airfoil Shape Parametrization Techniques for Early Design Optimization, AIAA Optimization Conference, September 2010. <https://doi.org/10.2514/6.2010-9050>
- 3 Ferguson J., Multivariable Curve Interpolation, Journal of the Association for Computing Machinery, 1964. <https://doi.org/10.1145/321217.321225>
- 4 Hicks R., Henne P., Wing Design by Numerical Optimization, Journal of Aircraft, 1978. <https://doi.org/10.2514/3.58379>
- 5 Farin G., Curves and Surfaces for Computer Aided Geometric Design, Academic Press, 1990.
- 6 Sobieczky H., Parametric Airfoils and Wings, Notes on Numerical Fluid Mechanics, 1998. https://doi.org/10.1007/978-3-322-89952-1_4

- 7 Kulfan B., Bussioletti J., Fundamental Parametric Geometry Representations for Aircraft Component Shapes, AIAA Multidisciplinary Analysis and Optimization Conference, 2006. <https://doi.org/10.2514/6.2006-6948>
- 8 Holmes P., Lumley J., Berkooz G., Turbulence and Coherent Structures Dynamical Systems and Symmetry, Cambridge University Press, 1996. <https://doi.org/10.1017/CBO9780511622700>
- 9 Nagarajan K., Cordier L., Airiau C., Kourta A., POD Based Reduced Order Modelling of a Compressible Forced Cavity Flow, French Congress on Mechnaics, 2009. <http://hdl.handle.net/2042/36791>
- 10 Rowley C., Colonius T., Murray R., POD Based Models of Self-Sustained Oscillations in the Flow Past an Open Cavity, AIAA Aeroacoustics Conference, AIAA Paper, June 2000. <https://doi.org/10.2514/6.2000-1969>
- 11 Cai X., Ladeinde F., A Comparison of Two POD Methods for Airfoil Design Optimization, AIAA Aviation, June 2005. <https://doi.org/10.2514/6.2005-4912>
- 12 Iuliano E., Quagliarella D., Aerodynamic Shape Optimization via non-instrusive POD-based Surrogate Modelling, IEEE, June 2013. doi: 10.1109/CEC.2013.6557736.
- 13 Kennard R. W., Stone L. A., Computer Aided Design of Experiments, Technometrics, April 2012. <https://doi.org/10.2307/1266770>
- 14 Iuliano E., Global Optimization of Benchmark Aerodynamic Cases Using Physics-Based Surrogate Models, Aerospace Science and Technology, April 2017. <https://doi.org/10.1016/j.ast.2017.04.013>
- 15 Huntington D. E., Lyrntzis C. S., Improvements to and Limitations of Latin Hypercube Sampling, Probabilistic Engineering Mechanics, October 1998. [https://doi.org/10.1016/S0266-8920\(97\)00013-1](https://doi.org/10.1016/S0266-8920(97)00013-1)
- 16 İuliano E., Towards a POD-Based Surrogate Model for CFD Optimization, ECCOMAS Thematic Conference, May 2011
- 17 Kutkan H., Aerothermodynamic Shape Optimization Using DSMC and POD-RBF Methods, Master Thesis, July 2018
- 18 Rogers C. A., Kassab A. J., Divo A., Ostrowski Z., and Bialecki A., An Inverse POD-RBF Network Approach to Parameter Estimation in Mechanics, Inverse Probl. Sci. Eng., vol. 20, no. 5, pp. 749-767, 2012. <https://doi.org/10.1080/17415977.2012.693080>
- 19 Benaissa B., Köppen M., Wahab M. A., and Khatir S., Application of Proper Orthogonal Decomposition and Radial Basis Functions for Crack Size Estimation Using Particle Swarm Optimization, J. Phys. Conf. Ser., vol. 842, no. 1, 2017. <https://doi.org/10.1088/1742-6596/842/1/012014>
- 20 Caboni M., Minisci E., Riccardi A., Aerodynamic Design Optimization of Wind Turbine Airfoils Under Aleatory and Epistemic Uncertainty, Journal of Physics, 2018. <https://doi.org/10.1088/1742-6596/1037/4/042011>
- 21 Mishra A. A., Mukhopadhaya J., Iaccarino G., Alonso J., An Uncertainty Estimation Module for Turbulence Model Predictions in SU2, AIAA, 2018. <https://doi.org/10.2514/1.J057187>
- 22 Emory M., Pecnik R., Iaccarino G., Modeling Structural Uncertainties in Reynolds-Averaged Computations of Shock/Boundary Layer Interactions, AIAA Aerospace Sciences Meeting, January 2011. <https://doi.org/10.2514/6.2011-479>
- 23 Xiao H., Wu J.L., Wang J.X., Sun R., Roy C. J., Quantifying and reducing model-form uncertainties in Reynolds-averaged Navier-Stokes simulations: A data-driven, physics-informed Bayesian approach, Journal of Computational Physics, August 2016. <https://doi.org/10.1016/j.jcp.2016.07.038>
- 24 Choi H. J., Allen J. K., Rosen D., McDowell D. L., Mistree F., An Inductive Design Exploration Method for Robust Multiscale Materials Design, ASME, September 2005. <https://doi.org/10.1115/1.2829860>
- 25 Choi H. J., Allen J. K., Rosen D., McDowell D. L., Mistree F., An Inductive Design Exploration Method for the Integrated Design of Multi-scale Materials and Products, ASME, September 2008. <https://doi.org/10.1115/DETC2005-85335>
- 26 Jang S., Choi H. J., Choi S. K., Oh J. S., Inductive Design Exploration Method with Active Learning for Complex Design Problems, Applied Science, October 2018. <https://doi.org/10.3390/app8122418>
- 27 Kumar Y., Srivastava S. K., Bajpai A. K., Kumar N., Development of CAD algorithms for Bezier Curves/Surfaces Independent of Operating System, WSEAS Transactions on Computers, 2012
- 28 Sirovich L., Chaotic dynamics of coherent structures, Physica, 1997. [https://doi.org/10.1016/0167-2789\(89\)90123-1](https://doi.org/10.1016/0167-2789(89)90123-1)
- 29 Newman A. J., Model Reduction via the Karhunen-Loeve Expansion Part I: Exposition, 1996. <http://hdl.handle.net/1903/5751>
- 30 Deane A. E., Kevrekidis I. G., Karniadakis G. E., Orszag S. A., Low-Dimensional Models for Complex Geometry Flows: Application to Grooved Channels and Circular Cylinders, Physics of Fluids A: Fluid dynamics, 3(10), 2337-2354. <https://doi.org/10.1063/1.857881>

- 31 Iuliano E., Quagliarella D., Aerodynamic Shape Optimization via Non-Intrusive POD-Based Surrogate Modelling, IEEE Congress on Evolutionary Computation, June 2013.
<https://doi.org/10.1109/CEC.2013.6557736>
- 32 Kern P. C., Priddy M. W., Ellis B. D., McDowell D. L., pyDEM: A generalized implementation of the inductive design exploration method, Materials and Design, August 2017.
<https://doi.org/10.1016/j.matdes.2017.08.042>
- 33 Afzal A., Kim K.-Y., Seo J.-W., Effects of Latin hypercube sampling on surrogate modeling and optimization, International Journal of Fluid Machinery and Systems, Vol.10, No. 3, July-September 2017.
<https://doi.org/10.5293/IJFMS.2017.10.3.240>
- 34 Yildirim B. Y., Tuncer İ. H., Hesaplamalı Akışkanlar Dinamiği ve Cevap Yüzey Yöntemi Kullanılarak Kanat Tasarımının Eniyilemesi, UHUK, September 2020
- 35 Anderson J., Aircraft Performance and Design, McGraw-Hill, 1999, Chapter 5, pg. 199-319
- 36 Economon T. D., Palacios F., Copeland S. R., Lukaczyk T. W., Alonso J. J., SU2: An Open-Source Suite for Multiphysics Simulation and Design, AIAA, December 2015. <https://doi.org/10.2514/1.J053813>
- 37 Jameson A., Analysis and Design of Numerical Schemes for Gas Dynamics Artificial Diffusion, and Discrete Shock Structure, International Journal of Computational Fluid Dynamics, September 1994.
<https://doi.org/10.1080/10618569508940734>
- 38 Wen-long W., Hua L., and Sha P., Performance Comparison and Analysis of Different Schemes, and Limiters, International Journal of Physical and Mathematical Sciences, Vol:5, No:7, 2011.
- 39 Menter P. R., Two-Equation Eddy-Viscosity Turbulence Models for Engineering Applications, AIAA Paper 93-2906. 1993. <https://doi.org/10.2514/3.12149>
- 40 Schulze D., Far Field Boundary Conditions Based on Characteristic and Bicharacteristic Theory Applied to Transonic Flows, 14th International Conference on Numerical Methods in Fluid Dynamics, 2005.
https://doi.org/10.1007/3-540-59280-6_124
- 41 Akossou A. Y. J., Palm R., Impact of Data Structure on the Estimators R-Square and Adjusted R-Square in Linear Regression. <http://hdl.handle.net/2268/155316>
- 42 Giunta A. A., Aircraft multidisciplinary design optimization using design of experiments theory and response surface modeling methods, Ph.D. Dissertation, Department of Aerospace Engineering, Virginia Polytechnic Institute and State University, Blacksburg, VA, May 1997
- 43 Sandia National Laboratories, DAKOTA, a multilevel parallel object-oriented framework for design optimization, parameter estimation, uncertainty quantification, and sensitivity analysis, Technical Report, May 2016
- 44 Jang S., Choi H. J., Choi S. K., Oh J. S., Inductive Design Exploration Method with Active Learning for Complex Design Problems, Applied Sciences, November 2018. <https://doi.org/10.3390/app8122418>
- 45 Marler R. T., Arora J. S., Survey of multi-objective optimization methods for engineering, Springer, September 2002. <https://doi.org/10.1007/s00158-003-0368-6>
- 46 Rao J. R., Roy N., Fuzzy set theoretic approach of assigning weights to objectives in multicriteria decision making, International Journal of Systems Science, April 1988. <https://doi.org/10.1080/00207728908910222>